

RESEARCH ARTICLE

WILEY

Numerical investigation of the influence of shear and thermal stratification on the wind turbine tip-vortex stability

Amy Hodgkin¹  | Sylvain Laizet¹  | Georgios Deskos² 

¹Department of Aeronautics, Imperial College, London, UK

²National Wind Technology Center, National Renewable Energy Laboratory, Golden, Colorado, USA

Correspondence

Amy Hodgkin, Imperial College, London, UK.
Email: a.hodgkin19@imperial.ac.uk

Funding information

Engineering and Physical Sciences Research Council, Grant/Award Number: EP/R029326/1; Imperial College London; Partnership for Advanced Computing in Europe AISBL, Grant/Award Number: 2019215138; Wind Energy Technologies Office; Alliance for Sustainable Energy, LLC, for the U.S. Department of Energy (DOE), Grant/Award Number: DE-AC36-08GO28308

Summary

The interaction between wind turbine wakes and atmospheric turbulence is characterised by complex dynamics. In this study, two major components of the atmospheric boundary layer dynamics have been isolated, namely, the mean velocity profile shear and the thermal stratification, to examine their impact on the near-wake development by undertaking a series of highly resolved large-eddy simulations. Subsequently, instantaneous flow fields are extracted from the simulations and used to conduct Fourier analysis and proper orthogonal decomposition (POD) and compute the mean kinetic energy fluxes by different POD modes to better understand the tip-vortex instability mechanisms. Our findings indicate that shear can significantly affect the breakup of the wind turbine tip-vortices and the shape and stable length of the wake, whereas thermal stratification seems to only have limited contribution to the spatial development of the near-wake field. Finally, our analysis shows that the applied perturbation frequency determines the tip-vortex breakup location as it controls the onset of the mutual inductance instability.

KEYWORDS

near-wake field, shear, stable wake length, thermal stratification, tip-vortex stability

1 | INTRODUCTION

Wind turbine wakes have been characterised as a major factor impacting the power output and structural health of large-scale wind farms.^{1,2} Turbine wakes are subject to a complex ambient environment, which is characterised by strong shear, veer, thermal stratification and terrain-specific large-coherent structures.³ Thermal stratification is one of the most fundamental atmospheric boundary layer (ABL) parameters, as it determines the mean velocity profile (shear) and the intensity and structure of turbulence.⁴ The effect of thermal stratification also classifies the atmospheric surface layer into a neutral, unstable (convective) and stable ABL. The latter category of the stable ABL occurs at nighttime when the ground is radiatively cooled and leads to stronger shear profiles and lower turbulence intensity.^{5–7} The combination of strong shear and a positive thermal stability has a profound effect on the wake length, strength and profiles.^{8–10} For instance, the large-eddy simulation (LES) study of Abkar and Porté-Agel¹¹ showed that the wake deficit of a single wind turbine increases with increasing atmospheric stability, whereas Magnusson and Smedman¹² reported the same behaviour using field measurements. In quantifying the wake characteristics (length, expansion etc.) under strong shear and thermal stratification, it is important to be able to identify a stable wake length, which is defined as the length of the wake region extending from the rotor plane, where helical vortex structures are shed from the blades' tips, to the location where the tip-vortex system breaks down to turbulence. As tip-vortices break up into smaller structures, the 'stable' wake field transitions to a far-wake field, which consists of

This is an open access article under the terms of the Creative Commons Attribution License, which permits use, distribution and reproduction in any medium, provided the original work is properly cited.

© 2022 The Authors. *Wind Energy* published by John Wiley & Sons Ltd.

smaller turbulent structures that are rapidly mixing with the ambient fluid.¹³ The magnitude of the stable wake length can be impacted by multiple factors, including thermal stratification and the mean shear profile.

The problem of wind turbine tip-vortex stability can be traced back to the seminal work of Havelock,¹⁴ who studied the stability of motion of rectilinear (line) vortices in a ring formation. Havelock's study considered a single ring formation with and without an assigned velocity field and the addition of an outer boundary (wall). The stability of a helical vortex filament of finite core and infinite extent to small sinusoidal displacements of its centre-line was many years later studied by Widnall.¹⁵ Her study identified three main modes of instability and classified them according to their perturbation frequency. These are the very short-wave instability, the mutual inductance instability and the long-wave instability. Of particular interest is the mutual inductance instability, which arises when vortex pairing occurs due to out-of-phase perturbation of tip-vortices and becomes prevalent as the pitch of the helix decreases. In a follow-up study, Gupta and Loewy¹⁶ considered the stability of a multiplicity of helical vortices to model tip-vortices of helicopter rotors, showing that the number of helices as well as their pitch and vortex core width all play an important part in the stability of the vortex system. The problem of helix vortex stability was recently revisited with both analytical^{17,18} and experimental studies¹⁹ which identified additional mechanisms for stable vortex breakdown states and their dependence on the vortex system characteristics.

Numerical investigations of tip-vortex stability have also been undertaken for simple uniform and sheared flow using the actuator line method.²⁰ Ivanell et al.²¹ used numerical modelling to further investigate the mutual inductance instability causing tip-vortex breakdown in a uniform flow by applying a harmonic excitation at the blade tips. With the aid of Fourier analysis, they quantified the growth of the perturbation and proposed an analytical model to predict the stable wake length based on the operating conditions and the scaled growth rate of the perturbation. In a follow-up study, Sarmast et al.²² investigated the stability of wind turbine wakes using modal decomposition techniques, that is, proper orthogonal decomposition (POD) and dynamic mode decomposition. Their results confirmed that modes appear in pairs with the same energy content and spatial structure but with a phase shift. They proposed an analytical expression to compute the stable wake length based on the level of the ambient turbulence intensity. Later, an experimental investigation of the mutual inductance instability by Nemes et al.²³ using a three-blade hydrokinetic turbine and POD showed that the energy contribution of the POD modes decreases exponentially when ordered in terms of their descending eigenvalues. The eigenvalue of a mode is relevant because its magnitude, as a fraction of the sum of all eigenvalues, is equal to the percentage of energy that each mode contributes to the flow. More recently, Kleusberg et al.²⁴ investigated the tip-vortex breakup mechanisms of a single turbine in sheared flow up to 10%. They found that shear increases the stable wake length along the top and decreases it along the bottom and that the stable wake length expression of Sarmast et al.²² can still provide a good estimate when shear is present. The effect of kinetic energy transport and turbulence production within the shear layer of a turbine wake was recently investigated by Lignarolo et al.,²⁵ who examined the influence of the kinetic energy flux on the mutual inductance instability and highlighted its role in the onset of vortex distortion and breakdown, which enhances turbulent mixing and kinetic energy transport across the shear layer. De Cillis et al.²⁶ used numerical simulations and undertook POD analysis to identify the coherent structures in the wake of a turbine with and without a supporting tower structure and further quantified their contribution to break up of the tip-vortex system using the mean kinetic energy (MKE) entrainment of each POD mode as their indicator. Their results provided useful insight by relating specific POD modes with distinct flow features, such as the helical tip-vortex spirals, von-Karman vortices (due to the tower) and Kelvin-Helmholtz instability (due to wake shear layer). Their study also supported earlier findings by Lignarolo et al.,²⁵ who suggested that the helical spiral mode has a negative MKE flux, preventing helical vortices from breaking down to smaller turbulent structures. Conversely, the tower has had a positive MKE flux, thus contributing to the wake's breakdown to turbulence.

In this numerical study, the problem of wind turbine tip-vortex stability is revisited by shifting our focus to the combined effects of shear and thermal stratification under a fully controlled and idealised scenario. Our model serves as a simplified version of the turbulent conditions experienced by utility-scale wind turbines and aims at extracting information germane to the stability mechanisms inherent to the wind turbine, helical, tip-vortex system. It is also an extension of the work performed by Ivanell et al.,²¹ Sarmast et al.²² and Kleusberg et al.²⁴ For our analysis, we use highly resolved flow field snapshots obtained by means of scale-resolving simulations. The obtained data are subsequently analysed with Fourier series, POD of the flow field and by computing the MKE fluxes. To this end, the remainder of this paper is organised as follows. Section 2 introduces the flow solver, simulation setup and data-analysis methods and provides a short validation study. Section 3 presents the results starting with a qualitative assessment of the vorticity field and the wake area followed by Fourier analysis, global and local POD and eventually the computation of the MKE fluxes. At the end, we discuss the main findings of this numerical study in Section 4.

2 | METHOD

2.1 | Flow solver

The turbulence-resolving simulations (LES) presented in this numerical study are performed with the high-order finite-difference wind farm simulator WInc3D,²⁷ which is part of the open-source framework of flow solvers Xcompact3D.²⁸ For our simulations, we use the implicit large-eddy simulation (iLES) approach of Dairay et al.,²⁹ which has been previously used to resolve wind turbine wakes.³⁰ The equations governing the

dynamics of the wind turbine wake are the unsteady, three-dimensional, incompressible, Navier–Stokes equations given in a non-dimensional form,

$$\frac{\partial u_i}{\partial x_i} = 0, \quad (1a)$$

$$\frac{\partial u_i}{\partial t} = -\frac{1}{2} \left(u_j \frac{\partial u_i}{\partial x_j} + \frac{\partial u_i u_j}{\partial x_j} \right) - \frac{\partial p}{\partial x_i} + \frac{1}{Re} \mathcal{D} + F_i, \quad (1b)$$

$$\frac{\partial \theta}{\partial t} = -u_j \frac{\partial \theta}{\partial x_j} + \frac{1}{Re \cdot Sc} \mathcal{Q}, \quad (1c)$$

where u_i is the velocity vector field, p is the pressure field, θ is the potential temperature and F_i accounts for additional forcing (with $i = 1, 2, 3$ corresponding to the streamwise (x), vertical (y) and spanwise (z) directions, respectively), $Re = U_0 R / \nu$ is the Reynolds number based on the reference free-stream velocity (U_0), the turbine radius (R) and the kinematic viscosity (ν), and Sc is the Schmidt number. As no reference to a particular explicit filter is made or written for Equation (1), the variables u_i, p and θ should be interpreted as the grid-resolved variables. The subgrid scales are modelled by the hyper-viscous momentum diffusion term, \mathcal{D} , which is defined as

$$\mathcal{D} = \frac{\partial^2 u_i}{\partial x_j \partial x_j} + \frac{\partial}{\partial x_j} \left(Q_c \star \frac{\partial u_i}{\partial x_j} \right), \quad (2)$$

where Q_c is a hyper-viscous kernel used to construct an iLES operator through a convolution operation (\star). Further details are not provided here for space considerations, but the interested reader is referred to the referenced studies^{29–31} for more information about this LES technique. One thing we should emphasise however is that the present iLES approach is based on a strategy that introduces targeted numerical dissipation at the smaller scales through the discretisation of the second derivatives of the viscous terms and does not involve the convective term (e.g. through upwinding). Nonetheless, the amount of numerical dissipation that is added to the flow is controlled by the parameter ν_0/ν , which corresponds to the added dissipation at the cutoff wavenumber. For this study, we follow the recommendation that was set forward by Deskos et al.,³⁰ who determined that values $100 \leq \nu_0/\nu \leq 1000$ yield high-accuracy solutions for high Reynolds number flows. To this end, a value of $\nu_0/\nu = 500$ was selected after a preliminary study (not presented here) showed that the flow is not affected by the parameter ν_0/ν as long as $\nu_0/\nu > 500$. As far as the forcing term (F_i) is concerned, it includes the buoyancy (gravitational) and turbine forcing terms. The former is defined by the Boussinesq approximation so that the added gravitational force is equal to $g\Delta\theta/\theta_0$, where g is gravitational acceleration and θ_0 is the reference temperature, whereas the turbine forcing is modelled using a standard actuator line implementation.^{20,27}

The discretisation of the governing equations is done using sixth-order compact finite-difference schemes for the spatial derivatives and an explicit third-order Runge–Kutta scheme for time marching. The use of higher-order schemes necessitates special treatment of the non-linear term of the momentum equation, which is computed in the skew-symmetric form for increased stability and to reduce aliasing errors.³² Likewise, the non-linear transport term is evaluated in its non-conservative form due to the use of different types of boundary conditions for the density field and velocity fields. The temperature diffusion term (\mathcal{Q}) is defined in a similar fashion to the momentum diffusion term (\mathcal{D}); the operators for the derivatives in \mathcal{Q} are the same as the operators in \mathcal{D} . The Poisson equation, which guarantees the incompressibility of the velocity field, is fully solved in spectral space via the use of relevant three-dimensional fast Fourier transforms (FFTs). By using the concept of modified wavenumber,³³ the divergence free condition is ensured up to machine accuracy. The pressure mesh is staggered from the velocity mesh by half a node to avoid spurious pressure oscillations observed in a fully collocated approach.³⁴ The simplicity of the mesh allows an easy implementation of a two-dimensional domain decomposition based on pencils.³⁵ The computational domain is split into a number of subdomains (pencils), which are each assigned to a message passing interface (MPI) process. The derivatives and interpolations in the x -direction (y -direction, z -direction) are performed in X -pencils, Y -pencils and Z -pencils, respectively. The three-dimensional FFTs required by the Poisson solver are also broken down as series of one-dimensional FFTs computed in one direction at a time. Global transpositions to switch from one pencil to another are performed with the MPI command `MPI_ALLTOALL(V)`. Winc3D can scale well with up to hundreds of thousands of MPI processes for simulations with several billion mesh nodes.³⁵ Further details and extensive validation studies of this wind farm simulator can be found in referenced papers.^{27,30}

2.2 | Simulations setup

The simulations setup is based on a scale-model three-bladed turbine (with radius $R = 10.24$ m) from experiments conducted in the wind-tunnel at the Norwegian University of Science and Technology.³⁶ The computational domain has a total size $10R \times 10R \times 10R$, and the turbine is placed at mid-height $2R$ downstream of the inlet as shown in Figure 1 (left). The domain is discretised with a uniform mesh of $513 \times 513 \times 513$ nodes,

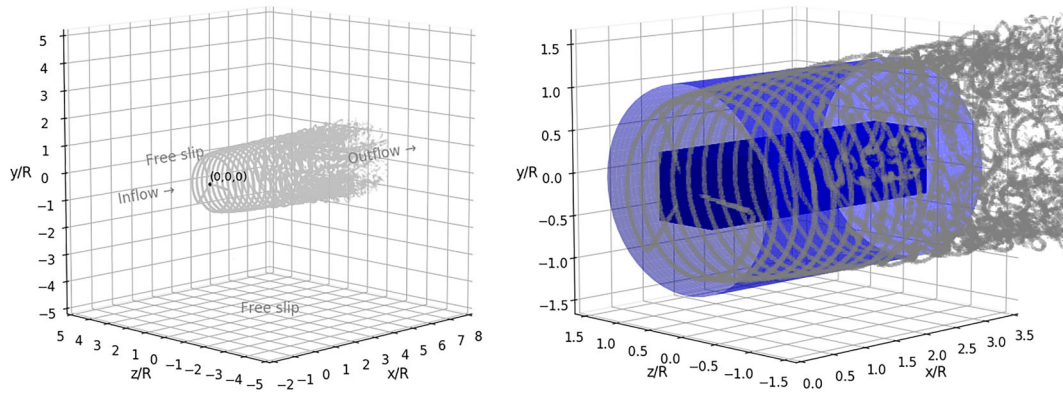


FIGURE 1 Left: Sketch of the computational domain with the turbines located at $(0, 0, 0)$. It is discretised with a uniform mesh of $513 \times 513 \times 513$ mesh nodes. Right: Control volume for the MKE flux calculation with $R_c = 1.2R$, and the root vortex removed (shown in dark blue)

giving a mesh resolution of $\Delta x = 0.02R$, which sufficiently resolves the blades and wake features. The resolution of the present study is similar to the resolution used in similar previous studies, see for instance.²⁴ The Reynolds number is equal to $Re = 30,000$ with a tip speed ratio ($\lambda = \Omega R / U_0$) of 6, where Ω is the angular velocity of the turbine.

The discretisation of the blades within the actuator line method use 100 blade elements and a look-up table specific to the turbine's airfoil characteristics to evaluate the lift, drag and pitch moment coefficients all based on the local Reynolds number. Additionally, a tip loss correction factor³⁷ is used near the tip of the blade. The actuator line forces are projected onto the fluid mesh with a smoothing parameter ($\epsilon = 2.2\Delta x$). For the velocity boundary conditions, we consider a free-slip in the vertical and spanwise directions and inflow/outflow boundary conditions in the streamwise direction with a uniform inflow velocity field applied at the inlet and a one-dimensional convection equation at the outlet to effectively convect the turbulent wake outside of our computational domain. The time step for the present simulation is 0.0005 s, which guarantees a Courant–Friedrichs–Lewy number < 0.1 . For our post-processing data analysis, we extract a total of 600 three-dimensional snapshots of the wake field at a frequency of 0.05 s after the wake is fully developed and stationarity of the turbulent flow is established. A preliminary study shows that mean statistics and POD modes are fully converged with as few as 600 snapshots and only a marginal difference of 1% between 600 and 1000 snapshots was observed.

To investigate the effect of shear on the turbine wake, a uniform velocity gradient can be set as

$$u_1(x, y, z) = U_0(ay + 1), \quad (3)$$

where $a = \partial u_1 / \partial y$ is the vertical velocity gradient. For this study, a takes values 0, 0.1 and 0.2, corresponding to a shear strength of 0%, 10% and 20%. These agree with shear levels experienced by modern large rotor blades in a neutral and stable boundary layer.¹¹ The effect of thermal stratification on the flow is also investigated by imposing a uniform positive vertical temperature gradient across the entire domain,

$$\theta(x, y, z) = \theta_0(by + 1), \quad (4)$$

where θ_0 is the reference temperature equals unity and $b = \partial \theta / \partial y$ takes the values 0, 0.01 and 0.02, resulting in vertical thermal stratification strengths of 0%, 1% and 2%. The applied gradient is maintained with top and bottom wall fixed-temperature boundary conditions equal to the initial values at these locations. For this study, the focus is on stable simulations (without a boundary layer) as they have been shown to have complex dynamics, requiring the most POD modes to recreate substantial energy in the flow³⁸ and present a problem to wind farm optimisation as they have lower power outputs than neutral and unstable setups. To destabilise the tip-vortices and trigger turbulence, the flow can be perturbed harmonically about the blade tip region. This is done by adding a body force to the streamwise (x -direction) momentum equation,

$$F_p = A \sin(k_p \Omega t), \quad (5)$$

where k_p is the non-dimensional perturbation wavenumber. The amplitude, $A = 0.13$, of the perturbation is chosen to match an equivalent maximum perturbation turbulence intensity of 0.5% near the perturbation location when no turbine is present. This turbulence intensity has been carefully chosen as it causes the breakdown of the helical vortices to occur within the studied domain (typically within a few radii downstream of the blades), and it also matches previous work.²¹ The perturbation is applied in a region extending 0.5R on either side of the rotor plane at either

side of the blade at all radii between $0.75R$ and $1.25R$. This idealised simulation setup allows us to study the individual influence of shear and thermal stratification on the tip-vortex dynamics, which would not be possible in turbulent or full boundary layer flow.

2.3 | Fourier analysis

Fourier analysis is used to study the response of the wake to the applied tip perturbation.²¹ Using Fourier series, the flow field is decomposed into its frequency components, also known as Fourier modes. The Fourier modes are extracted from the snapshots for the velocity magnitude ($u_{mag} = \sqrt{u_i^2}$) and over N_F snapshots via

$$\Phi_n = \frac{1}{N_F} \sum_{m=1}^{N_F} u_{mag,m} e^{-imn\frac{2\pi}{N_F}}, \quad (6)$$

where $i = \sqrt{-1}$, index m corresponds to the m th velocity magnitude field, index n refers to the n th Fourier mode, and N_F is chosen to capture a multiple of the full time period of the perturbation. The time period of the Fourier transformation is equal to $0.05N_F$, and for out-of-phase perturbations, the perturbation time period is equal to $2 \times$ the blade passing time period ($2T_b$). The mode for which $n = 0.05N_F/2T_b$ is the one capturing the dynamics of the perturbation frequency, and we denote this mode Φ_p . The maximum of Φ_p , as a function of streamwise distance, can be defined as

$$\widehat{\Phi}_p(x) = \max_{y,z} (|\Phi_p(x,y,z)|), \quad (7)$$

where $\widehat{\cdot}$ denotes the maximum value. This can then be used to evaluate the perturbation growth rate $\tilde{\sigma}$ obtained with

$$\tilde{\sigma} = \frac{d \log(\widehat{\Phi}_p)}{dx}. \quad (8)$$

2.4 | Proper orthogonal decomposition

POD is a modal decomposition technique that extracts coherent features of the flow by finding orthogonal basis vectors. The method of snapshots³⁹ provides a quick way to solve the eigenvalue problem to find POD modes. The method finds a set of orthonormal functions, ϕ_i^k , from which the complete velocity field, u_i , can be reconstructed

$$u_i = \bar{u}_i + \sum_{k=1}^N \phi_i^k a_k, \quad (9)$$

where $\bar{\cdot}$ indicates the averaged value over N snapshots, index k corresponds to the k th mode velocity field, ϕ_i^k is the velocity of mode k in direction i and a_k is the corresponding temporal coefficient (amplitude). The modes are ordered in terms of their energy contribution to the flow, with the most dominant (energetic) first.

2.5 | Mean kinetic energy flux

The contribution of each POD mode to the breakdown of the wake can be assessed by looking at the turbulent MKE flux, which is known to be the biggest contributor to the wake breakdown.^{40–42} This term is extracted from the transport equation for the MKE as

$$-\frac{\partial}{\partial x_j} (\bar{u}_i \overline{u_i' u_j'}),$$

with $\overline{u_i' u_j'} = \bar{u}_i \bar{u}_j - \bar{u}_i \bar{u}_j$. Hence, the turbulent MKE flux per unit area through a closed surface (S_c) can be found by integrating the term over the volume (V_c) enclosed by the surface via

$$\mathcal{F}_T = \frac{1}{S_c} \int_{V_c} -\frac{\partial}{\partial x_j} (\overline{u_i u_i' u_j'}) dV_c. \quad (10)$$

In the present work, the control volume is a cylinder ($V_c = \pi R_c^2 L_c$ and $S_c = 2\pi R_c L_c$) centred on the turbine location with length (L_c) and radius (R_c) with a cuboid of side length of $0.8R$ centred on the root vortex removed, as can be seen in Figure 1 (right) for $R_c = 1.2R$. The individual contribution of each POD mode can be assessed using the reconstruction in Equation (9), as described in De Cillis et al.²⁶ The turbulent MKE flux can be approximated with a finite set of modes as

$$\overline{u_i' u_j'} \approx \sum_{k=1}^N (a_k \phi_i^k) \sum_{l=1}^N (a_l \phi_j^l) = \sum_{k=1}^N \sum_{l=1}^N \overline{a_k a_l} \phi_i^k \phi_j^l = \sum_{k=1}^N \lambda_k \phi_i^k \phi_j^k, \quad (11)$$

where λ_k is the eigenvalue of mode k , which represents the strength of the k th mode. Following this, the total flux of MKE due to turbulent fluctuations for a single mode is

$$\mathcal{F}_T^k = \frac{1}{S_c} \int_{V_c} -\frac{\partial}{\partial x_j} (\overline{u_i \lambda_k \phi_i^k \phi_j^k}) dV_c. \quad (12)$$

The relationship between the local flux and the total flux is

$$\mathcal{F}_T^k = \int f_T^k(x) dx; \quad (13)$$

hence, the local MKE flux, as a function of x , is found using

$$f_T^k(x) = \frac{1}{S_c} \int_{S_c} -\frac{\partial}{\partial x_j} (\overline{u_i \lambda_k \phi_i^k \phi_j^k}) dy dz. \quad (14)$$

2.6 | Validation study

A validation study is carried out against the results presented in Kleusberg et al.,²⁴ which investigates wind turbine wakes in uniform flow and flow with a shear strength of up to 10%. Their setup is very similar to the present one with the only difference being the choice of numerical methods, the size of the computational domain and the mesh resolution. Other parameters, such as the Reynolds number, blades and tip speed ratios, have all remained the same. With this setup, two simulations are performed for validation purposes in which a sheared flow of 0% and 10% is applied along with zero wavenumber perturbation ($k_p = 0$), and the radial vortex growth rate is compared with the reference data of Kleusberg et al.²⁴ The radial vortex growth rate, which corresponds to the radial extent of the wake as a function of the distance downstream of the blades, is found by plotting the length from the centre of the domain to the edge of the helical vortex. It is defined to include all mesh nodes with an average vorticity of at least 10 at 90° intervals around the computational domain. Present results are plotted along with those of Kleusberg et al.²⁴ in Figure 2, showing excellent agreement with only small differences observed, which can be attributed to the different numerical methods and the selected spatial resolution. The maximum error between the present results and the reference data is 2%, found at 180° (bottom) for 10% shear at $x = 3.1R$ downstream of the blades. Note that we have also examined the vortex growth rate for $k_p = 3/2$ with 0% and 10% shear, and an excellent agreement with the reference data was also obtained (not presented here for conciseness).

3 | RESULTS

A selection of results from a total of 27 simulations is presented in this paper. The simulations were performed with three different perturbation frequencies with $k_p = 0, 3/2$ and $9/2$, three different shear strengths (0%, 10% and 20%) and three different thermal stratification strengths (0%, 1% and 2%). Note that the case with no shear and no thermal stratification is referred to as the uniform case. Perturbation frequencies of $k_p = 3/2$ and $9/2$ were chosen as they give out-of-phase perturbations in which each vortex line interacts with both neighbours, with a time period of $2T_b$. These perturbation frequencies trigger the mutual inductance instability (vortex pairing), causing the wake breakdown. Similar

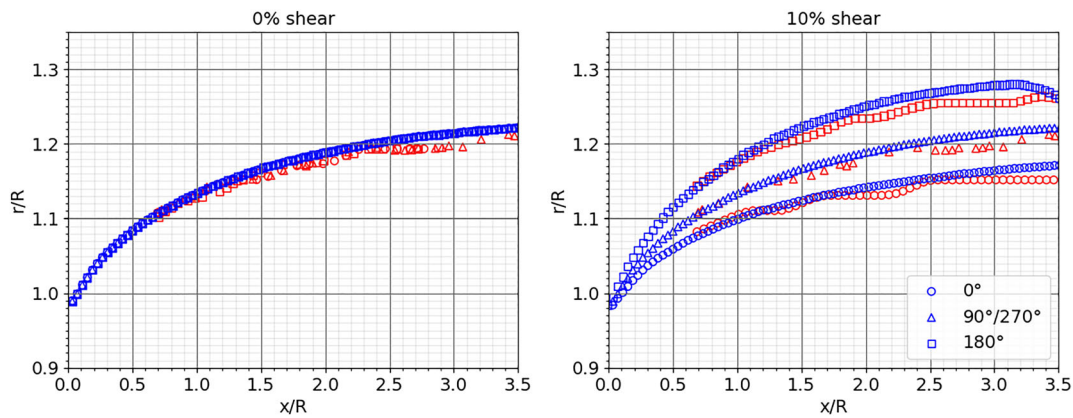


FIGURE 2 Streamwise evolution of the radial vortex growth for uniform flow (left) and with 10% shear (right) for $k_p = 0$ (no perturbation). Present data are in blue while the reference data of Kleusberg et al.²⁴ are in red. The angles refer to the top (0°), left/right ($90^\circ/270^\circ$) and bottom (180°) of the turbine wake

single frequency harmonic perturbations were used in Ivanell et al.²¹ and Kleusberg et al.²⁴ Preliminary simulations with frequencies of $k_p = 3$ and 4 were also performed. $k_p = 3$ corresponds to an in-phase perturbation, with no vortex pairing occurring in the computational domain of interest that results in wake evolution identical to that of the unperturbed case ($k_p = 0$). $k_p = 4$ is an in-partial-phase perturbation so vortex pairing occurs; however, the breakdown to turbulence is slower compared with out-of-phase perturbations. Shear and thermal stratification strengths were chosen to closely resemble values experienced by modern large-scale wind farms in neutral and stable boundary layers,¹¹ as discussed in the introduction section.

3.1 | Vorticity field and wake area

The development of turbine wakes can be visualised by looking at the vorticity magnitude up to $3.5R$ downstream of the turbines, in the present study, as seen in Figure 3, for the simulations without thermal stratification. Without perturbation ($k_p = 0$) or shear, the wake can be characterised by a helical spiral that gradually expands radially as it evolves downstream of the turbines without breaking down to turbulence for the computational domain of interest. The addition of an out-of-phase perturbation causes the helical spiral to break up as the perturbation grows, caused by vortex pairing, for example, see the case with $k_p = 3/2$ and no shear. The vortex pairing is caused by the mutual inductance instability, triggered by the perturbation at the blade tips. It can be seen in Figure 3 that the breakup location, where the helical vortices start to interact together, depends on the perturbation frequency. The cases with $k_p = 3/2$ correspond to a large wavelength and consequently result in a rather early breakup as the amplitude of the perturbation grows quickly, irrespective of the shear strength. The cases with $k_p = 9/2$, with a smaller wavelength, take longer for the perturbation amplitude to reach a level large enough to cause vortex pairing and trigger the transition to turbulence.

The shear strength also affects the transition to turbulence. It acts to lengthen the stable wake length along the top and shorten it along the bottom. A consequence of shear is that the helical vortices are convected faster at the top than at the bottom, as clearly seen in cases where a zero perturbation is applied. As a result, the spacing between vortex lines, also called the streamwise vortex separation distance, at the top is larger than the one at the bottom, with vortex pairing first occurring at the bottom where the vortex lines are closer to each other. For the case with $k_p = 0$ and 20% shear, the transition to turbulence is happening from around $2R$ downstream of the turbine at the bottom, whereas no transition is observed with a 10% shear profile. For perturbed cases, the breakup of the tip-vortices occurs after the same number of rotations for all vortex filaments, but because the lines are slanted and the streamwise vortex separation distance is greater at the top, the top of the turbine wake does not transition to turbulence within the computational domain of interest. The perturbed cases in Figure 3 also suggest that the mechanisms behind the transition to turbulence are likely to be different with and without shear, which will be confirmed later in this article by means of Fourier analysis and POD of the velocity field. In the far-wake field the turbulent structures become smaller and less recognisable as the flow continues to break down to smaller structures, with interaction of helical tip and root vortices. These small structures start to dissipate, with an increased rate of mixing with the ambient. For cases with perturbations, the imprint of the mutual inductance instability can be seen up to the end of the computational domain (not shown here for brevity) as the vortical structures are grouped in a number of ‘lobes’ relating to the wavelength of the perturbation.

To visualise the effect of thermal stratification and to better understand the effect of the applied perturbation at the blade tips, the helical vortices can be plotted as planar vortex lines in the (θ, x) plane, as shown in Figure 4. The vortex lines are cut along the top, flattened out and plotted as a function of their downstream position from the turbines. Each plot corresponds to a perturbation and shear strength with or without

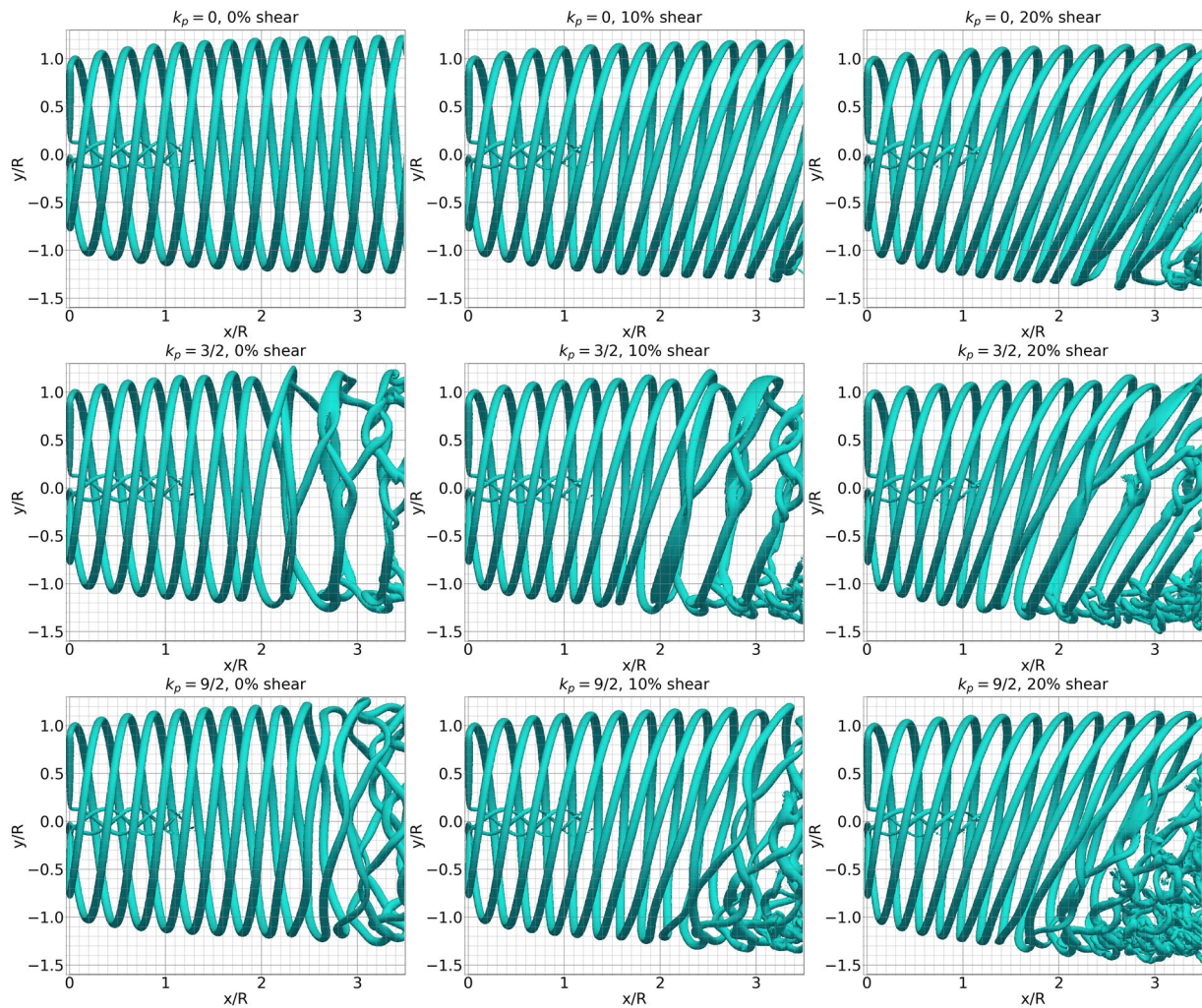


FIGURE 3 Development of the helical vortices for the cases with no thermal stratification, shown with an isocontour of the vorticity magnitude $\omega = 15.65$

thermal stratification. Dashed lines on the plot divide the wake into linear, transition and turbulent regions, as defined for the no-shear case. These regions are used in subsequent analysis. The linear region is defined from $0.5R$ to remove any root-vortex effects. The transition region begins at the first sign of oscillation of the vortex lines (at $1.5R$ for $k_p = 3/2$ and $1.8R$ for $k_p = 9/2$). Once the vortex lines have interacted with each other (crossed), the turbulent region begins (at $2R$ for $k_p = 3/2$ and $2.8R$ for $k_p = 9/2$). The streamwise extent of the transition region for $k_p = 3/2$ is half that of the $k_p = 9/2$ one, confirming that the transition to turbulent is happening faster for $k_p = 3/2$. The mutual inductance instability can be seen clearly for the 0% shear cases, where the vortex lines, which are initially parallel, start to interact with each other. The vortex pairings can clearly be seen in this figure and the imprint of the perturbation. For the cases with no shear and $k_p = 3/2$, three vortex pairing regions are initiated for $\theta = 105, 225, 345^\circ$, while nine vortex pairing regions can be observed for $k_p = 9/2$. Interestingly, the imprint of the perturbation is weaker when the shear is increased with only one dominant pairing region around $\theta = 180^\circ$ for both perturbations (corresponding to the bottom of the wake). The most notable result in Figure 4 is that the thermal stratification seems to have a negligible effect on the breakup of the tip-vortex system and its transition to turbulence. The dominant factors affecting the breakdown to turbulence are the shear strength and the magnitude of the frequency of the perturbation at the blade tips. In fact, adding thermal stratification only marginally alters the shape of the planar vortex lines, with a slight earlier destabilisation of the tip-vortices when thermal stratification is added to the flow. This trend is consistent with Figure 5, in which a slight increase of the perturbation growth is reported when thermal stratification is added to the flow. These trends might be counter-intuitive with results observed in the ABL where stable thermal stratification can delay the transition to turbulence of turbines wakes by suppressing turbulence. In the present idealised setup, with no boundary layer or wall effects, thermal stratification does not have the ability to suppress the wall shear stresses leading to reduced turbulence levels.⁴³ For cases with no shear, an unstable profile could be observed by flipping the computational domain upside down. Hence, the sign of the thermal stratification alone does not have opposite impacts on the streamwise location of the transition to turbulence as we do not have a boundary layer.

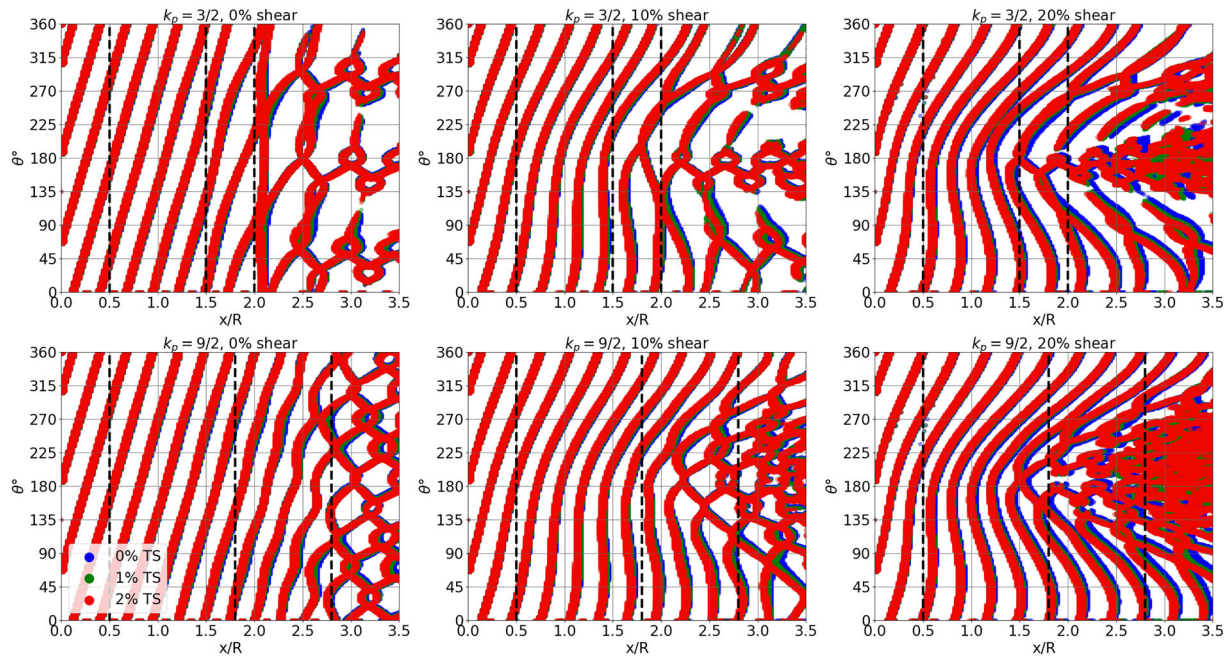


FIGURE 4 Planar vortex lines for $k_p = 3/2$ (top) and $k_p = 9/2$ (bottom) with 0% shear (left), 10% shear (middle) and 20% shear (right). Blue, green, red colours correspond to 0%, 1%, 2% thermal stratification, respectively. Dashed lines mark the start of the linear, transition and turbulent regions

The shape of the wakes can be seen in Figure 5 at three different streamwise locations downstream of the turbines for all 27 cases. The boundary of the wake is found by computing the convex hull of all points with a mean vorticity ($\bar{\omega}$) ≥ 4.5 . Note that the boundary and the shape of the wake are impacted by the applied perturbation forcing, often leading to an irregular pattern, depending on the perturbation wavelength. At a distance of $1R$ downstream of the turbines, the perturbation does not cause a big difference in the wake shape. The wake has a circular shape with a radius of about $1.15R$ and the effect of thermal stratification is still not detectable. With increasing shear, the shape of the wake is changed from strictly circular to ellipsoidal. The lateral dimensions of the wake in shear are the same as the cases with no shear, but the wake extent at the top is marginally reduced while it is increased up to $1.3R$ at the bottom, with a downward shift of the centre of the ellipse. The effect of thermal stratification can only be seen at the bottom of the wake with an increase of the wake extent when thermal stratification is added to the flow. It should be noted that the difference in the wake shapes at $1R$ between the cases with thermal stratification strengths of 1% and 2% are negligible. Further downstream, at a distance of $2R$ from the turbines, the imprint of the perturbation can clearly be seen, especially for the cases with $k_p = 3/2$. The effect of the thermal stratification here is more pronounced, particularly for the highest-shear-strength case and especially for the bottom half of the wake where an increase of its radius is observed. Conversely, changes in wake radius for the top half of the wake are still small when thermal stratification is present. Finally, at a distance of $3R$ downstream of the rotor plane, it is clear that the centre of the wake has been shifted downwards as a result of the applied shear. The largest wake expansion is observed for the cases with the $k_p = 9/2$ and shear levels of 20%. If no shear is applied to the background flow, thermal stratification has very little to no influence on the wake shape, which is found to be dominated by the magnitude of perturbation frequency. This suggests that thermal stratification may not impact the breakup of the turbine tip-vortices, but it does affect the shape of the wake and therefore may influence the transition to turbulence and the dynamics of the far-wake field.

To quantify the effect of shear and thermal stratification, the wake area is calculated using the shoelace formula (Gauss's area formula). The percentage differences with respect to the uniform case are plotted in Figure 6 at a streamwise distance of $1R$, $2R$ and $3R$ downstream of the blades for each perturbation. The uniform case has the smallest area at each location, hence why it is used as the reference value. The computed percentage differences confirm our qualitative observation that shear and thermal stratification act to increase the area of the wake. The largest percentage difference from the uniform cases are reported for 20% shear + 1%/2% thermal stratification with an increase of the wake area of more than 15% for $k_p = 9/2$. The increase of the wake area is less important when thermal stratification is removed (for $k_p = 9/2$), confirming that thermal stratification impacts the evolution of the wake more importantly when shear is present. With no shear and thermal stratification, the increase of the percentage differences is minimal. It suggests that there is a strong connection between shear and thermal stratification, which affects the dimension of the wake, irrespective of the perturbation. Another interesting result for $k_p = 3/2$ is that the percentage difference for the wake area is bigger at $2R$ than it is at $3R$ downstream of the turbines, implying that the growth rate of the wake is slowing down between those two locations, which is not the case for $k_p = 9/2$. Finally, there is a significant increase of the wake area when the shear strength is increased from 10% to 20%.

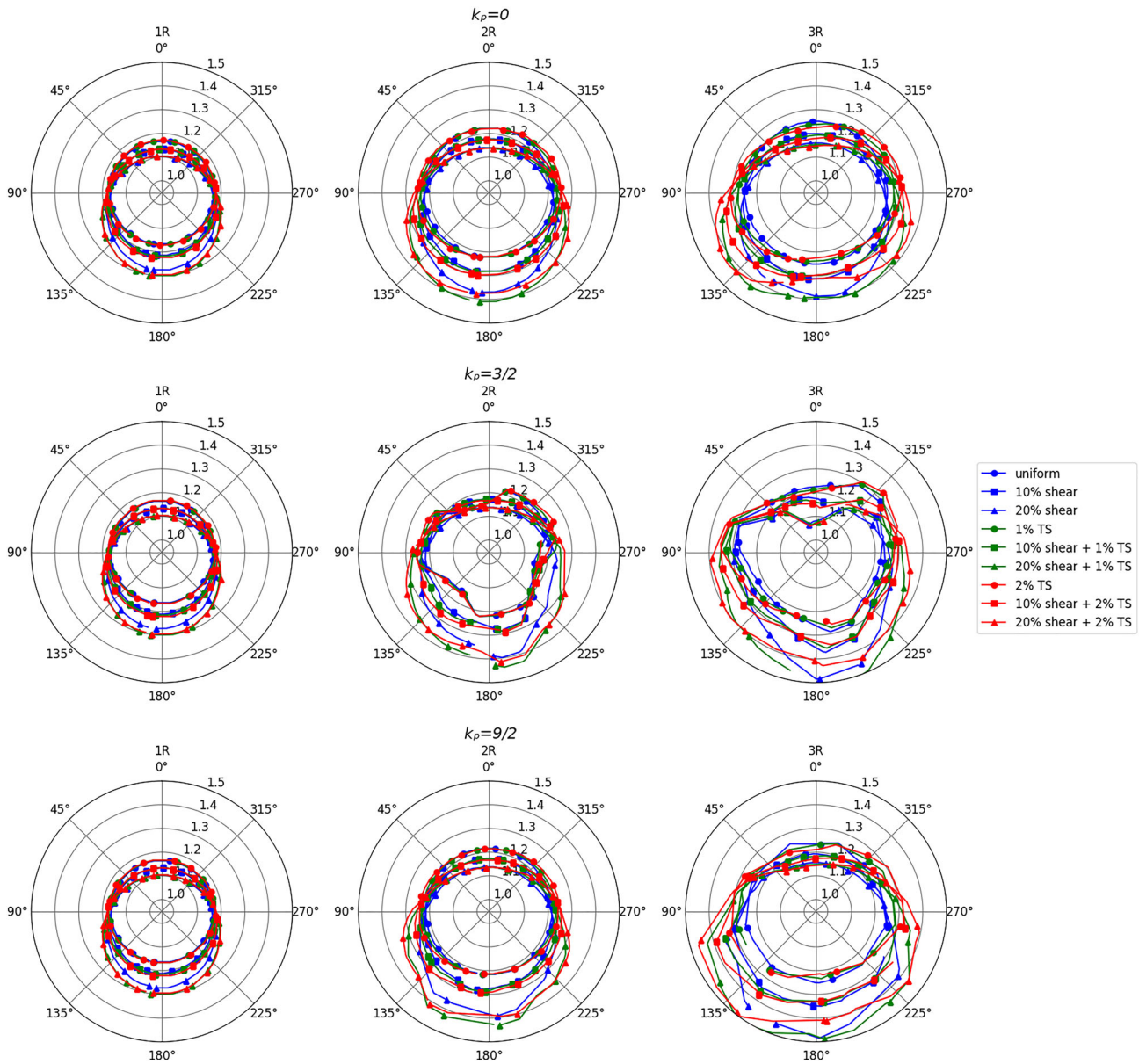


FIGURE 5 Shape of the wakes defined by the convex hull containing all mesh nodes with respect to the mean vorticity magnitude $\bar{\omega} \geq 4.5$, in the $y-z$ plane at three streamwise locations downstream of the turbine. Circle, square and triangle symbols correspond to 0%, 10% and 20% shear, respectively. Blue, green and red colours correspond to 0%, 1% and 2% thermal stratification, respectively

3.2 | Fourier response

As already reported by Ivanell et al.²¹ and Kleusburg et al.,²⁴ the added perturbation imposed at the blade tips grows exponentially after a brief period of receptivity. An example of the transition from the linear to the turbulent regions is presented in Figure 7. As the perturbation travels along the helical vortices, the amplification of the perturbation causes distinct lobes to be formed in the flow field, with each lobe relating to half a wavelength of the perturbation. The location of each lobe can be found using the POD analysis, which will be presented next in Section 3.3. As the lobes are located at the boundary of the wake, they are amplified differently depending on the perturbation. To this end, we use Fourier analysis to investigate the effect of shear and thermal stratification on the spatial development of the perturbation. Our method, however, differs from that of Ivanell et al.²¹ as a fixed time between saved snapshots is used for our analysis. In order to properly isolate the perturbation response, it is necessary to select a number of snapshots with a total time period as close as possible to a multiple of the perturbation period. For all cases, 25 snapshots ($N_F = 25$) are selected to capture $4 \times 2T_b$ with an error of 0.15%, hence the fourth Fourier mode isolates the perturbation dynamics. The growth rate of the perturbation for each lobe is found following the method presented in Section 2.3.1, with $\Phi_p = \Phi_4$, by computing the

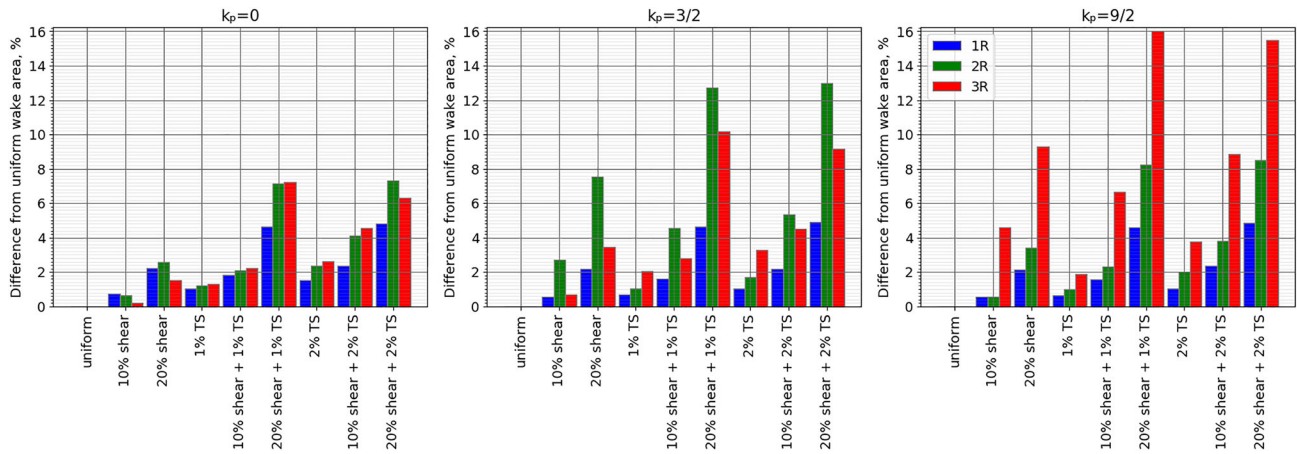


FIGURE 6 Percentage difference from the uniform wake area for each case at 1R (blue), 2R (green) and 3R (red) downstream of the turbine

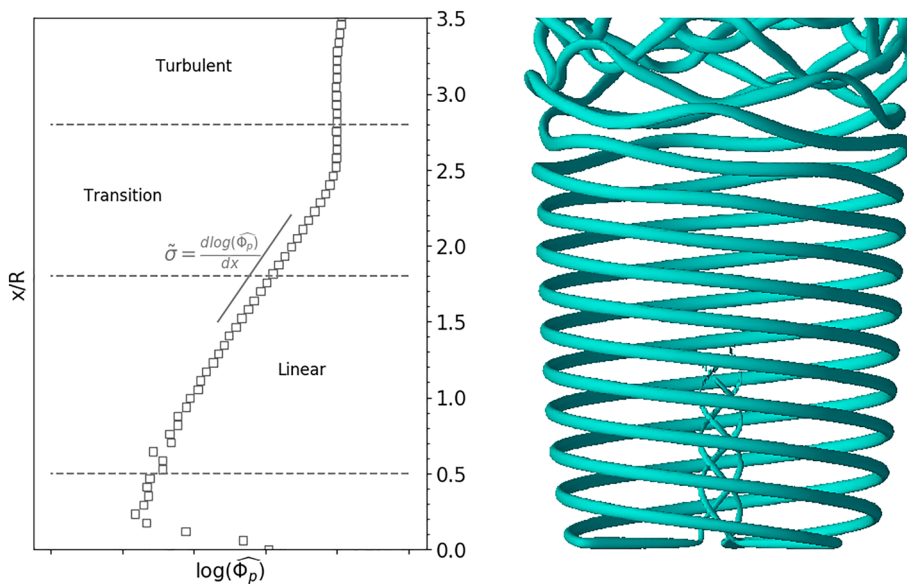


FIGURE 7 Development of $\widehat{\Phi}_p$, the maximum of the perturbation Fourier mode magnitude, on a log plot against streamwise distance from the turbine (the growth rate is the gradient of the linear portion). The wake can be visualised on the left to show where the perturbation growth is linear compared to the wake development. The example shown is for $k_p = 9/2$ with a uniform flow

maximum for slices in the (y,z) plane, each encapsulating a lobe. Figure 7 shows the shape of the maximum of the magnitude of this mode on a log plot compared with the vorticity magnitude to show the wake evolution. The streamwise dimensions related to the linear, transition and turbulent regions are also labelled in the figure. An initial settling period can be seen between 0 and $0.5R$. After this the perturbation starts to grow and becomes exponential (linear on the log plot) between $0.5R$ and $2.5R$. The exponential response of the perturbation is between the linear and transition regions as defined on the diagram. At about $2.5R$ downstream of the turbine, the response tails off, triggering the end of the transition region and the start of the turbulent region. Once the wake is turbulent, the magnitude of the mode increases again but at a very slow rate, suggesting that its imprint is not the dominant mechanism driving the evolution of the wake.

The left-hand side of Figure 8 shows the isolated POD mode related to the perturbation, which shows the distinct lobes and their radial positions (this mode is also shown in Figure 9). The growth rate for each lobe is displayed in the right-hand side of Figure 8 for $k_p = 3/2$ and $k_p = 9/2$. Note that the growth rate of each lobe is plotted at its centre. Due to the number of cases, the gradient is found automatically using a script that calculates the gradient of all sections of $0.5R$ length from $0.5R$ to $3.5R$ using linear regression. To capture the linear portion of the response, gradient values with a regression coefficient larger than 0.99 are selected and the average is found. To ensure the most accurate solution, values that fall outside of ± 1 standard deviation are then removed and the average is computed again. Note that the final value for the standard deviation over the mean of the gradients is <0.1 for all cases. It can be seen that the location of the lobes corresponds to the location of

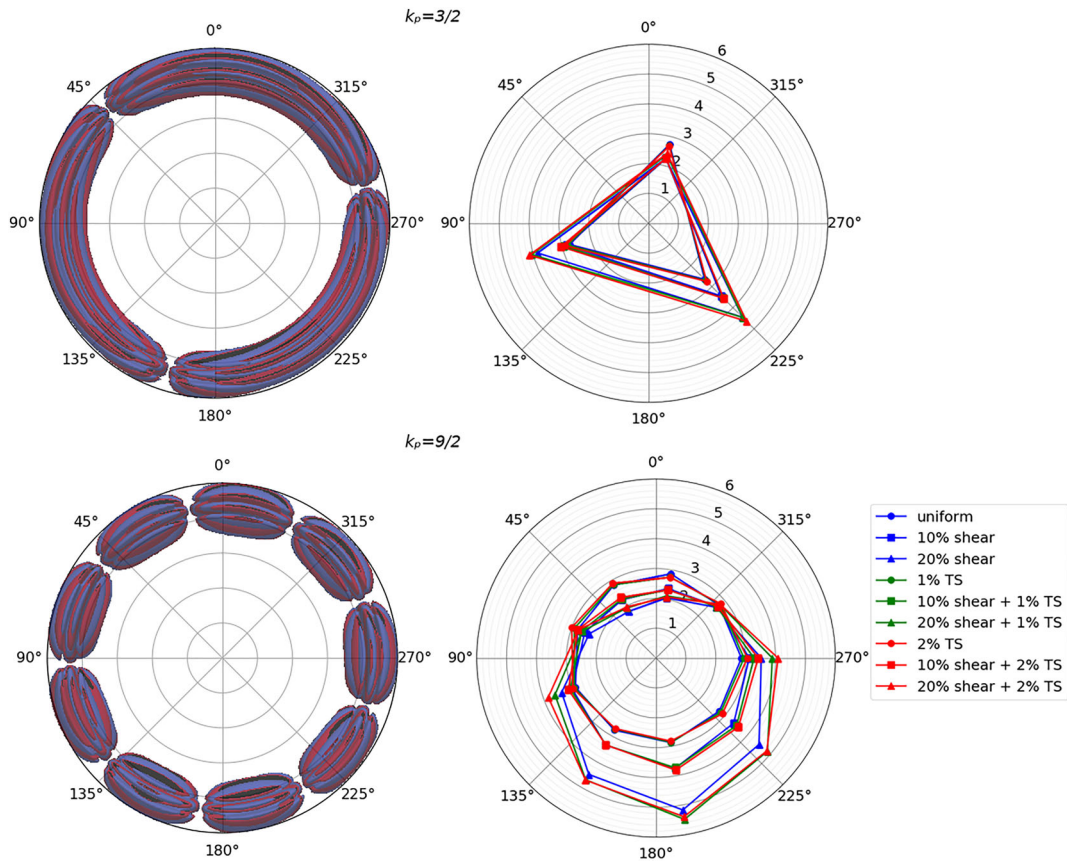


FIGURE 8 Polar plot of the growth rate, $\bar{\sigma}$, of each lobe, with three lobes for $k_p = 3/2$ (top) and nine lobes for $k_p = 9/2$ (bottom) with and without shear and thermal stratification. The angle refers to the radial position around the turbine with 0° corresponding to the top of the wake. The shape of the lobes (mutual inductance POD mode) is displayed on the left, with red showing a positive isocontour and blue showing a negative isocontour. Circle, square and triangle symbols correspond to 0%, 10% and 20% shear, respectively. Blue, green and red colours correspond to 0%, 1% and 2% thermal stratification, respectively

the vortex pairings observed in Figure 4. As expected with no shear and no thermal stratification, the growth rate is radially the same as the perturbation is growing with the same intensity around the rotor. For $k_p = 3/2$, the growth rate is about 2.7 and for $k_p = 9/2$, it is 2.8. For $k_p = 9/2$, this rate is about 0.5 larger than the growth rates reported by Kleusberg et al.,²⁴ but in our simulations, the breakdown to turbulence is happening sooner (by about one vortex rotation), hence the larger growth rate. However, it should be noted that the trends are similar. Shear increases the growth of the perturbation near the bottom and decreases it near the top, relative to the growth rate of the uniform case, with our rates remaining about 0.5 larger than comparison results.²⁴ The effect of thermal stratification is much smaller than the effect of the shear, and it is mainly influencing the sides of the wake (around 90° and 270°). The growth rate for each lobe is different as the lobes are not arranged symmetrically with respect to the vertical direction. The highest growth rate is therefore observed for the lobes located the closest to 180° as the shear is the dominant mechanism contributing to the growth rate of the perturbation. Differences are more visible for the $k_p = 9/2$ case, as the large number of lobes provides more information regarding the growth of the perturbation. As already discussed, the effect of the thermal stratification is more pronounced when the shear is strong. It should be noted, however, that the small differences in growth rate because of the applied thermal stratification profile do not affect the tip-vortex breaking mechanism.

3.3 | Proper orthogonal decomposition

In this subsection, a POD analysis is used to offer insight into how shear and thermal stratification affect the wake shape and ultimately the instability mechanism. POD modes are calculated for the full near-wake region ($0.5R - 3.5R$) for visualisation and analysis of the POD modes after removing from our analysis the root vortex. Subsequently, we calculate the POD modes for the linear, transition and turbulent regions. We should note that the location and streamwise extent for these regions are different for each perturbation frequency.

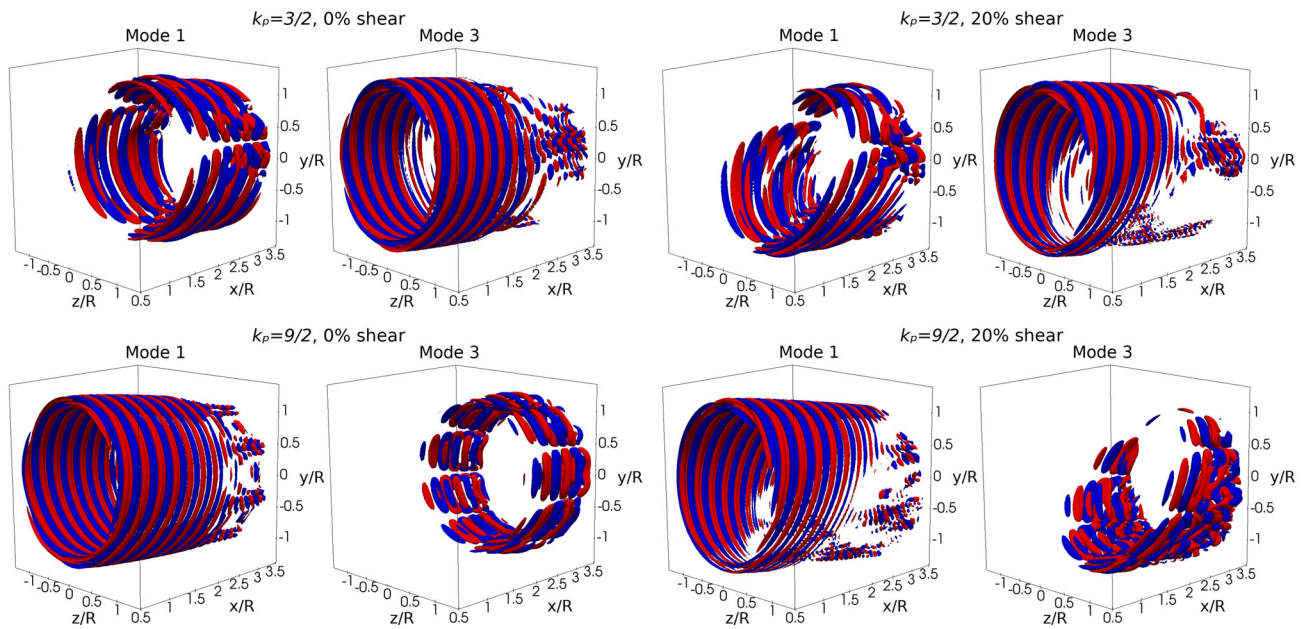


FIGURE 9 Structure of first two mode pairs - shown is mode 1 and mode 3 for $k_p = 3/2$ and $k_p = 9/2$. The first two mode pairs correspond to a helical spiral (mode 3 for $k_p = 3/2$ and mode 1 for $k_p = 9/2$) and the mutual inductance instability (mode 1 for $k_p = 3/2$ and mode 3 for $k_p = 9/2$). There are either 3 or 9 lobes depending on the perturbation. Red corresponds to a positive isocontour, and blue corresponds to a negative isocontour

3.3.1 | Full wake: 0.5R– 3.5R

Figure 9 shows the shape of mode 1 and 3 (i.e. the shape of the first two mode pairs; only one POD mode of each pair is shown for conciseness) for the perturbed cases with 0% and 20% shear. The POD modes with thermal stratification are not shown as they are virtually the same as the ones with no thermal stratification. The first two mode pairs (modes 1–2 and 3–4) correspond to a helical spiral pair (generated by the tip of the blades) and a pair forming the mutual inductance instability (generated artificially via the perturbation at the blade tips). The main difference between the two perturbation frequencies is that, for $k_p = 3/2$, the mutual inductance pair is the most energetic pair (pair 1, modes 1–2) whereas for $k_p = 9/2$ the helical spiral is the most energetic pair (pair 1, modes 1–2). As already seen in the previous section, the mutual inductance instability modes have distinct lobes, which relate to half a wavelength, with three lobes for $k_p = 3/2$ (pair 1, modes 1–2) and nine lobes for $k_p = 9/2$ (pair 2, modes 3–4). Figure 9 shows that the mutual inductance modes are more visible towards the end of the studied computational domain, whereas the helical spiral modes are more pronounced at the start of the computational domain (during the receptivity period for the perturbation). As a result, the shear is primarily affecting the mutual inductance pair of POD modes for both perturbation frequencies and then the helical spiral pair of POD modes. The mutual inductance instability modes are elongated at the bottom of the computational domain and are barely visible at the top of the domain. We also note that the shapes of the mutual inductance modes and helical spiral modes are similar to the one observed in Sarmast et al.²² for their flow configuration.

The energy content of a mode is found using the eigenvalue of that mode as a percentage of the total sum value of the eigenvalues. Due to the nature of the wake, transitioning from a laminar state to a turbulent state, the first two pairs of modes (modes 1–2 and 3–4) always contribute to at least 80% of the total energy of the flow. Figure 10 shows the energy percentage of the first 10 pairs of modes, with the most dominant pair of modes at the bottom in red and the 10th most dominant pair of modes at the top in blue. Inherently, the uniform flow case has the highest cumulative energy for the first 10 pairs of modes, reaching almost 100% of the total energy, as the wake only becomes turbulent at the very end of the computational domain of interest. Shear alone decreases slightly the cumulative energy. For the cases with thermal stratification but not shear, there is a small reduction in the total energy from the first 10 pairs of modes. The combination of 20% shear + 1% thermal stratification is the one for which the first 10 pairs of modes have the least cumulative energy (94% for $k_p = 3/2$ and 91% for $k_p = 9/2$). It suggests that this combination of shear and thermal stratification generates the most complex flow out of the different configurations studied in the present investigation. As a side note, the combination of 20% shear + 1% thermal stratification resembles the values observed in a stable boundary layer,¹¹ so they are representative of a practical setup of turbines in a wind farm. In line with our results, it was found recently that a stable boundary layer requires significantly more POD modes than neutral or convective boundary layers to capture the same energy content.³⁸ Finally, we note that the energy percentages obtained for the high-frequency perturbed cases of $k_p = 9/2$, produce marginally lower cumulative energy when compared to that of $k_p = 3/2$.

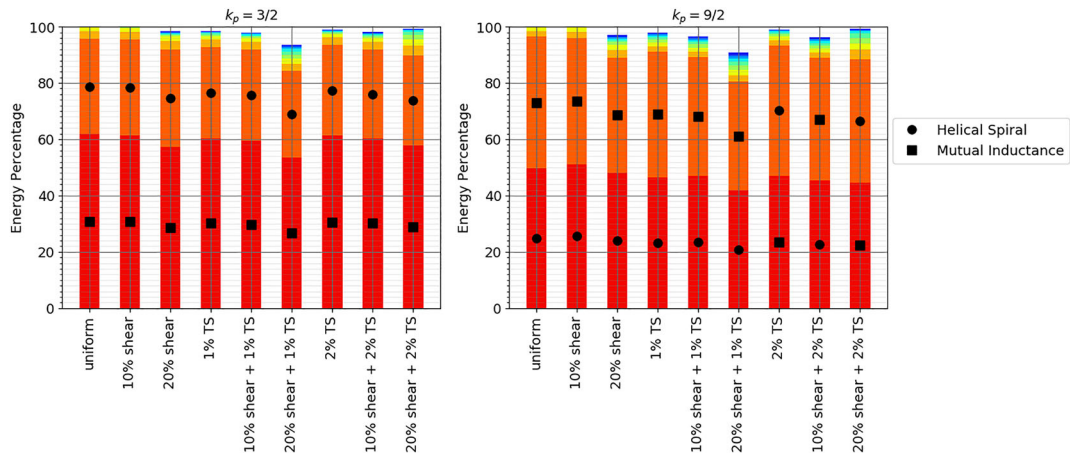


FIGURE 10 Energy percentage for the first 10 pairs of modes for the perturbed cases. The modes are ordered in terms of energy percentage, with the most dominant at the bottom of the plots in red

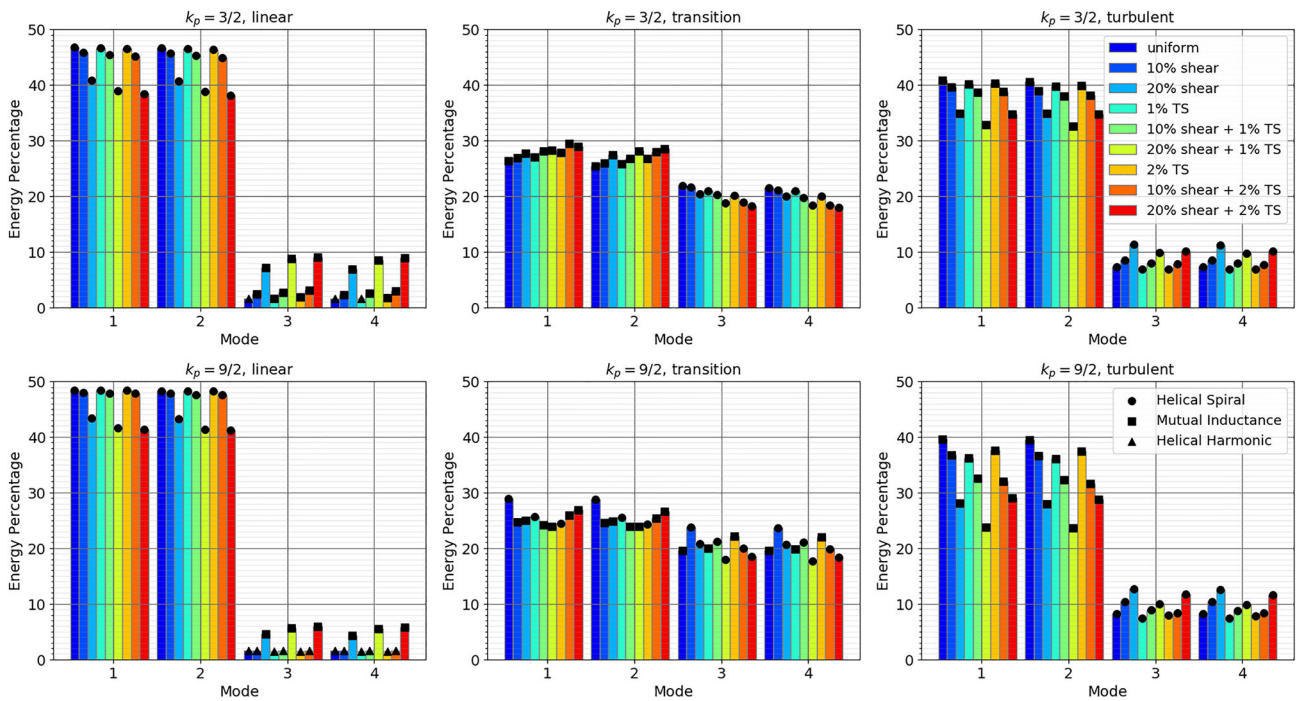


FIGURE 11 Energy percentage for POD modes for the linear, transition and turbulent regions. The type of POD modes is indicated at the top of the bars with a symbol: circle for the helical spiral, square for the mutual inductance instability and triangle for the helical spiral harmonic

3.3.2 | Linear, transition and turbulent regions

The full domain POD data give us a general indication of the overall coherent structures and their respective energy content. However, as the wake is transitioning from its laminar state to a turbulent state, it is instructive to perform a local POD analysis for the linear, transition and turbulent regions, as those were defined in Figure 4.

The percentage energy of the first four modes for each region is shown in Figure 11 for the cases with a non-zero perturbation frequency. The first four modes (two pairs of modes) constitute a helical spiral and the mutual inductance instability, except for a few cases in the linear region for which the second pair constitute a harmonic of the helical spiral. The shape of the mode is indicated by the symbol at the top of the bar (circle for the helical spiral pair of modes, square for the mutual inductance instability pair of modes and triangle for the helical spiral harmonic pair of modes). The evolution of the energy percentage for the POD modes when the wake is transitioning to turbulent is the same for all cases and can be summarised as follows. In the linear region, the helical spiral modes are dominant (circle symbols) with an energy percentage between 40%

and 50%, whereas the mutual inductance modes represent less than 10% of the total energy. In the transition region, the different dominant modes have more or less the same energy content between 20% and 30%, with slightly higher percentages for the mutual inductance modes, except for the uniform cases with $k_p = 9/2$. In the turbulent region, the mutual inductance modes are dominant (square symbols) with an energy percentage more or less between 30% and 40%, whereas the helical spiral modes represent about 10% of the total energy.

In the linear region, thermal stratification alone does not affect the energy percentages of the helical spiral and mutual inductance modes. When a high level of shear is added to the flow (20%), there is a reduction of the energy percentage of the helical spiral modes associated with an increase of the energy percentage of mutual inductance modes. Thermal stratification is amplifying this transfer of energy between different pairs of modes. As a result, the transition to turbulence is occurring earlier than in the uniform cases, as already noted in the discussion following Figure 3. These trends are the same for both perturbation frequencies, however they are more pronounced for $k_p = 3/2$. Finally, with no or less shear (i.e. 10%) and $k_p = 9/2$, the mutual inductance modes become less energetic than the modes associated with the harmonic of the helical spiral modes (triangle symbols). Still, these modes contain a very low energy content.

Moving on to the transition region, the effect of shear and thermal stratification is found to be less pronounced than in the linear region. Overall, the helical spiral modes are not the dominant modes anymore in term of energy content, except for very few cases with $k_p = 9/2$ with no shear. The energy content for both pairs of modes (helical spiral and mutual inductance instability) is more balanced than in the linear region, with values between 25% and 30% for the mutual inductance modes and around 20% for the helical spiral modes. Shear and thermal stratification increase the energy content of the mutual inductance modes and decrease the energy content of the helical spiral modes.

Finally, in the turbulent region, the mutual inductance instability modes are the most dominant mode pair for all cases. For $k_p = 3/2$, their energy percentage is higher than in the transition region, with values between 30% and 40% for $k_p = 3/2$ and values as low as 25% for $k_p = 9/2$. As in the linear region, shear acts to reduce the energy content of these modes, while thermal stratification alone has no effect, except when combined with shear. Note that the effect of shear and thermal stratification is more visible for $k_p = 9/2$, with fairly large differences in energy percentages for the mutual inductance modes (from 25% to 40%) when shear and thermal stratification are added to the flow. The lowest energy content for those modes is obtained for 20% shear + 1% thermal stratification, corresponding to the largest wake area, as demonstrated in Figure 5. The energy percentage for the helical spiral modes is around 10%, with higher values obtained when shear is added to the ambient flow.

3.4 | MKE flux of the POD modes

The MKE flux can be used to further investigate the effect of shear and thermal stratification on the near field evolution of wind turbines wakes. The contributions of the most dominant pairs of POD modes to the MKE flux are evaluated on a cylindrical control volume using the POD modes from $0R$ to $3.5R$ downstream of the turbines ($L_c = 3.5R$, shown in Figure 1 (right)). As it can be seen a square of side length $0.8R$ encapsulating the root vortex was removed for the POD calculations and hence is also removed for the MKE flux calculations.

Figure 12 shows the MKE flux for the first two dominant pairs of POD modes (helical spiral modes and mutual inductance modes) for the perturbed cases for a volume with radius $R_c = 1.2R$. The most dominant pair of modes are highlighted with a black circle symbol, whereas the

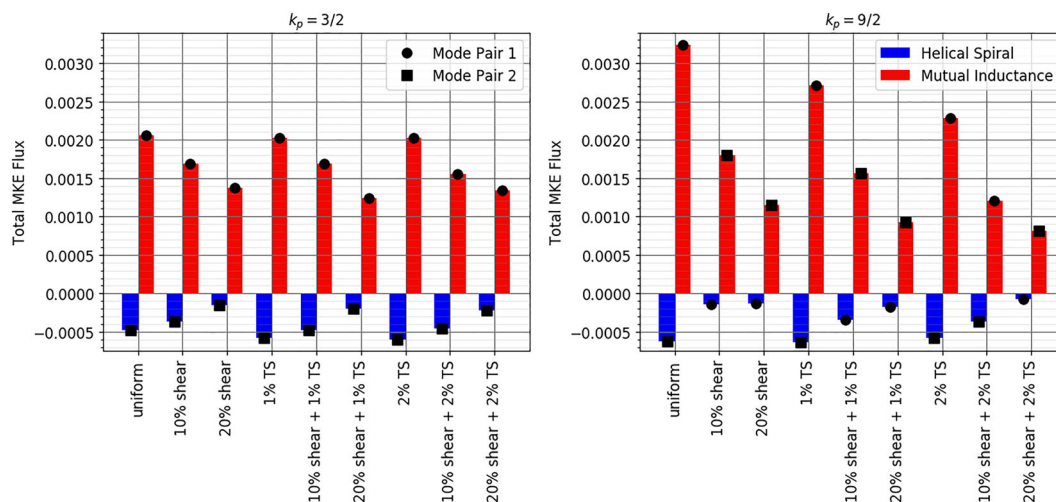


FIGURE 12 Total MKE flux (F_T for each setup for $k_p = 3/2$ and $k_p = 9/2$ for a control volume enclosing $R_c = 1.2$ and $x = 0-3.5R$. The first two dominant mode pairs are shown (the helical spiral in blue and the mutual inductance mode in red). The dominance of the mode pair is indicated by the circle for pair 1 and square for pair 2. Note that there is slight difference in the order compared with Figure 10 as the domain for the POD analysis and MKE analysis differ

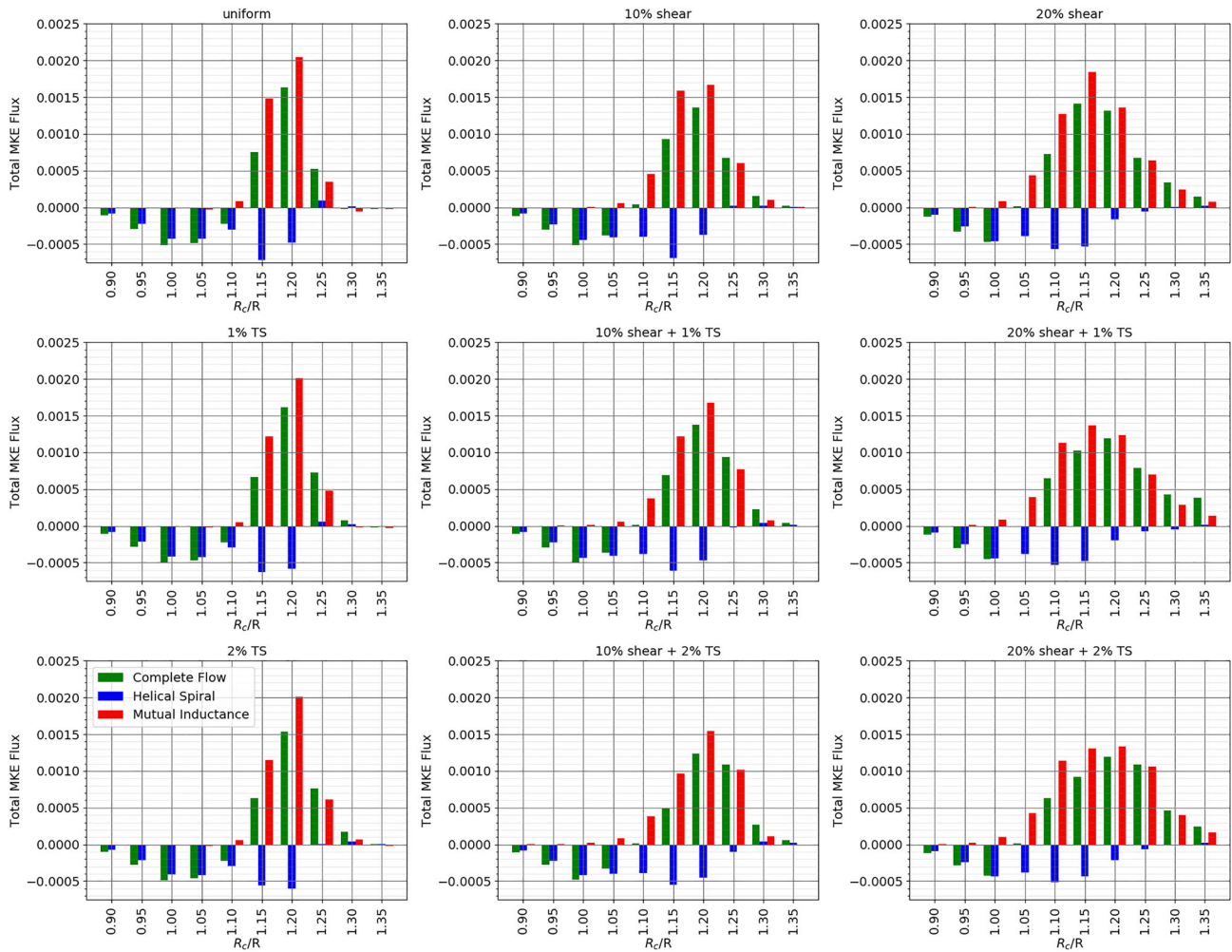


FIGURE 13 Total MKE flux for each setup with $k_p = 3/2$ for a varying control volume by altering R_c from 0.9R to 1.3R. $L_c = 3.5R$ and starts at the turbine hub ($x = 0$). The total MKE flux for the complete flow (\mathcal{F}_T) is in green, for the helical spiral (F_T^{HS}) is in blue, and for the mutual inductance instability (F_T^{MI}) is in red

second most dominant pair of modes are highlighted with a black square symbol. It can be seen that the mutual inductance pair of POD modes is always positive (in red) and is often the dominant mode (black circle symbol), except for a few cases when $k_p = 9/2$. The helical spiral pair of POD modes is always negative with a magnitude more or less three to five times less important than the magnitude of the flux from the mutual inductance pair of POD modes. A positive flux corresponds to a transfer of energy from the ambient fluid to the wake. It suggests that tip-vortices inhibit turbulent mixing (preventing the wake to transition to a turbulent state) and that the onset of the mutual inductance instability is the main triggering mechanism to turbulence. When shear is added to the flow, the magnitude of the fluxes is decreased for both mode pairs, suggesting that the helical pair of POD modes is less efficient at delaying the wake's transition to turbulence. The magnitude of MKE flux of the mutual inductance pair is also reduced, however it is still much bigger than the helical spiral pair, hence still the main contributor to triggering the breakup of the tip-vortices and their transition to turbulence. Another interesting result is that the amplitude of the MKE flux is more important for $k_p = 9/2$ than for $k_p = 3/2$, where the effect of the shear is amplified. On the other hand, the effect of thermal stratification on the MKE flux is marginal for both perturbations, with and without shear, especially for $k_p = 3/2$. For $k_p = 9/2$, thermal stratification contributes to the reduction of the amplitude of the MKE flux but not as much as the reduction associated with shear.

Figure 13 shows the total MKE flux for the velocity field (complete flow) and the helical spiral and mutual inductance instability pair of POD modes for $k_p = 3/2$. Note that the trends reported in this figure are similar for $k_p = 9/2$ (not shown here for brevity). In this figure, the data are plotted for a control volume with radii from 0.9R to 1.35R, with increment of 0.05R, and length of 3.5R from $x = 0$ downstream of the turbines. The amplitudes of MKE flux for the complete flow are dominated by the sum of the amplitudes of MKE flux from the two most dominant pair of POD modes (as their energy content is always around 80% of the total energy content of the flow). It is found that the maximum MKE flux of the complete flow and the mutual inductance instability pair of modes at any radii is obtained for the uniform flow setup, at 1.2R. The impact of shear

is to reduce this global maximum and increase the spread of MKE flux with radius, especially at higher radii. This can be explained by an increase in turbulence activity around the wake edges with less intense, less localised fluxes (the energy of the wake is spread out).

The MKE flux of the mutual inductance instability pair is negative up to a radial distance after which it switches to positive and grows. The radius at which this change occurs depends on the shear and thermal stratification intensity. For instance, under a uniform flow, this radius is found to be $R_c = 1.1R$ for $k_p = 3/2$ and $R_c = 1.15R$ for $k_p = 9/2$. Thermal stratification acts towards decreasing the radius at which the value switches from negative to positive. This coincides with a slight shift of the maximum MKE flux to the right and a larger flux is found at larger radii, that is, the weight of the curve shifts to the right. Likewise, for 20% shear, the peak moves from $R_c = 1.2R$ with no thermal stratification, to $R_c = 1.3R$ when the ambient temperature gradient is 1% and 2%.

The flux from the helical spiral modes reaches a local minimum usually at $R_c = 1R$ and then reaches its global minimum at $R_c = 1.15R$ (for $k_p = 3/2$) and $R_c = 1.2R$ (for $k_p = 9/2$) before growing again and switching positive at $R_c = 1.25R$. Shear shifts these minima to the left. Thermal stratification reduces the magnitude of the minima as it flattens them out, for example, for the case with 10% shear + 2% thermal stratification the first local minimum is very small. This is also evident from the $k_p = 3/2$ cases. The mutual inductance instability is centred around the helical spiral so that the difference in wake expansion between different cases (Figure 5) impacts the MKE flux for different control volumes. Figure 14 shows the magnitude of the vorticity field in the (y,z) plane for 1.5R– 3.5R downstream of the turbine for the 20% shear + 1% thermal stratification case with $k_p = 3/2$. A circle with radius of 1.2R is plotted for reference. It can be seen that the top of the wake is below the black circle while the bottom of the wake is outside the black circle, with small turbulent structures. It suggests that transfers of energy via the MKE flux might predominantly happen at the bottom of the wake, assuming that the small, energetic, turbulent structures are responsible for most of the mixing between the ambient and the wake.

Comparing with the results of De Cillis et al.,²⁶ it is found that the local MKE flux for the helical spiral is always negative at $R_c = 1R$ and experiences a large minimum peak in the first 0.25R downstream of the turbine. The influence of the mutual inductance instability mode at $R_c = 1R$ is very small, as it becomes dominant once the vortex has expanded outside of a radius $R_c = 1R$. At $R_c = 1.2R$, the local MKE flux of the helical spiral pair is mostly negative but does experience oscillations around zero towards the second half of the domain. The local MKE flux of the mutual inductance instability pair is larger in magnitude at this radius and remains zero up to some value (near the beginning of transition region) where it becomes positive. It oscillates to a small negative minimum before going positive again for 0% and 10% shear, whereas for 20% shear, the local flux of the mutual inductance mode is found to always be positive.

4 | CONCLUSIONS

In this numerical study, 27 high-fidelity simulations of a model turbine wake were generated using the actuator line method to assess the effect of shear and thermal stratification on the near-wake field vortex dynamics. In order to trigger the breakup of the tip-vortices into smaller scale turbulence, a single harmonic perturbation with different wavelengths was applied at the blade tips to promote the mutual inductance instability. To this end, we extracted instantaneous vorticity fields, undertook Fourier analysis, conducted local and global POD of the velocity fields as well as computed the MKE fluxes to obtain a complete and detailed picture of the underlying physical mechanisms that drive the near-wake dynamics. Our simulation setup allowed us to study the influence of shear and thermal stratification on the tip-vortex dynamics through idealised flow conditions. As such, it does not fully represent the ambient flow conditions of utility-scale wind turbines in the ABL. Nevertheless, our idealised model is capable of reproducing the instability dynamics inherent to the wind turbine's helical tip-vortex system, and thus shed light into the transition mechanisms from the near- to the far-wake field.

The application of harmonic tip perturbations leads to a near-wake breakdown in specific locations where the vortex filaments oscillate and interact. The number of breakdown locations depends on the perturbation frequency. Our analysis shows that thermal stratification does not impact the location where the near-wake breaks down to turbulence. On the other hand, ambient shear is found to largely determine the breakup location as it affects the spacing between helical vortex filaments, that is, shortening the helical vortex pitch at the bottom causing an earlier local breakdown. Inherently, this phenomenon increases the stable wake length at the top and reduces it at the bottom. Conversely, both thermal stratification and shear affect the area of the wake. More specifically, shear increases the wake area by increasing its radius at the bottom, whereas thermal stratification increases the wake radius at the sides. The effect is also more pronounced when thermal stratification is combined with strong shear. The difference in the wake area between the uniform flow and the combined sheared and thermally stratified flow can be as large as 16% for the case with 20% shear + 1% thermal stratification, compared to 9% for the respective shear-only case.

Apart from the geometry changes of the wake, certain dynamical characteristics are affected by the applied perturbation frequency and the ambient flow. Fourier analysis of the wake velocity fields showed that the perturbation frequency, controlled by the wavenumber is a key parameter in triggering and accelerating the mutual inductance instability after a receptivity period and the initial vortex pairing. The growth rate of the perturbation along the tip-vortices correlates with the wake shape, as we see in the planar vortex lines, with shear being larger at the bottom where we first observe the breakdown. Again, thermal stratification causes a slight increase in the growth rate, which correlates with the slightly earlier disruption of vortex lines, particularly at the sides.

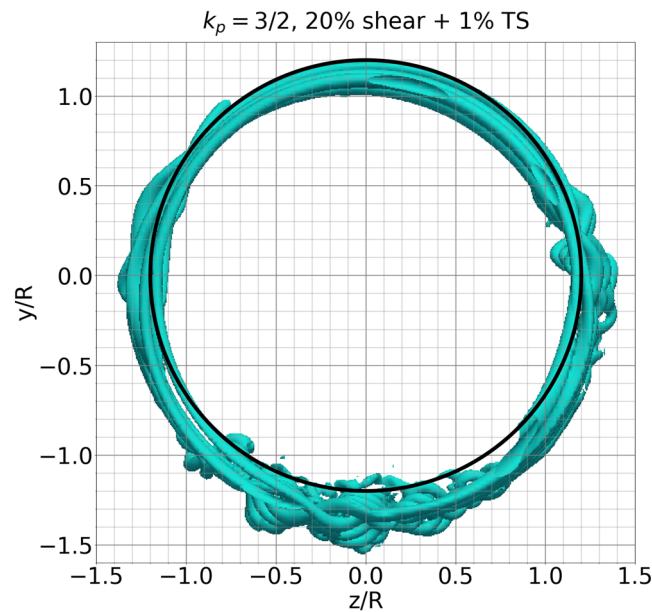


FIGURE 14 Vorticity magnitude of 15.65 for the case with $k_p = 3/2$, 20% shear + 1% thermal stratification in the (y, z) plane, showing the $R_c = 1.2R$ control volume circular area cross section for $1.5R - 3.5R$ downstream of the turbine

Further analysis using the POD method showed that the wake is made up of two dominant mode shapes (at least 80% of flow energy): the helical spiral and the mutual inductance modes, both driving the wake evolution. The helical spiral mode is dominant in the first half of the studied domain where the wake is laminar and the perturbation effects are not yet visible. On the other hand, the mutual inductance mode dominates further downstream and leads to the breakup of the tip-vortex system. Shear and thermal stratification do not significantly change the shape of these two modes, apart from causing the helical spiral to slant (shear) and altering the mode area in line with the wake area. Nevertheless, the energy content of these modes changes with shear and thermal stratification. Interestingly, the least cumulative energy in a finite set of modes is found for the cases with 20% shear + 1% thermal stratification, indicating the most complex flow setup in terms of energy in structures.

The impact of the two dominant coherent structures was also studied through their mode-dependent MKE flux. It was found that the helical spiral mode exerts a shielding effect on the wake by delaying the breakdown to turbulence, whereas the mutual inductance instability mode has the opposite effect, promoting fluxes between the wake and its ambient. The magnitude of these effects is diminishing with increasing shear and, to a lesser extent, with thermal stratification. Finally, shear and thermal stratification reduce the fluxes of the mutual inductance instability modes but increase the MKE flux at larger radii.

In summary, the key finding of our study is that shear has a much larger impact on the near-wake dynamics and wake shape than thermal stratification, although some results, particularly those on the wake shape, suggest that shear and thermal stratification need to be investigated together to obtain the full picture. Nevertheless, we expect that the wake area could have a significant follow-on impact to the far-wake field. The difference between 1% and 2% thermal stratification is less important than the difference between no thermal stratification and some thermal stratification. Yet a stable thermal stratification profile alone does not slow down the perturbation growth, as is the case in a stable boundary layer where wall shear stresses are present. Recognising the complexity of the ABL, future work would focus on the influence of additional effects present in a stable boundary layer, such as veer and wall effects, amongst others. Additionally, dynamic control strategies that focus on reducing the stable wake length are of particular interest as their role is to mimic the application of harmonic tip perturbations for faster wake recovery.

ACKNOWLEDGEMENTS

The authors thank the Engineering and Physical Science Research Council for the computational time made available on the UK supercomputing ARCHER facility via the UK Turbulence Consortium (EP/R029326/1). Computational time was also provided by the Partnership for Advanced Computing in Europe via the Irene-Rome supercomputer facilities (grant number: 2019215138). The authors would like to acknowledge the Department of Aeronautics, Imperial College London for supporting this work funded by a doctoral studentship. Finally, G. D. would like to acknowledge funding from the U.S. Department of Energy (DOE). This work was authored in part by the National Renewable Energy Laboratory, operated by Alliance for Sustainable Energy, LLC, for the U.S. Department of Energy (DOE) under Contract No. DE-AC36-08GO28308. Funding provided by the U.S. Department of Energy Office of Energy Efficiency and Renewable Energy (EERE), Wind Energy Technologies Office (WETO).

The views expressed in the article do not necessarily represent the views of the DOE or the U.S. Government. The U.S. Government retains and the publisher, by accepting the article for publication, acknowledges that the U.S. Government retains a nonexclusive, paid-up, irrevocable, worldwide license to publish or reproduce the published form of this work, or allow others to do so, for U.S. Government purposes.

PEER REVIEW

The peer review history for this article is available at <https://publons.com/publon/10.1002/we.2728>.

DATA AVAILABILITY STATEMENT

The data are available on request from the authors.

ORCID

Amy Hodgkin  <https://orcid.org/0000-0002-6596-0286>

Sylvain Laizet  <https://orcid.org/0000-0003-0346-0662>

Georgios Deskos  <https://orcid.org/0000-0001-7592-7191>

REFERENCES

1. Thomsen K, Sørensen P. Fatigue loads for wind turbines operating in wakes. *J Wind Eng Ind Aerodyn*. 1999;80(1):121-136.
2. Barthelme RJ, Pryor SC, Frandsen ST, et al. Quantifying the impact of wind turbine wakes on power output at offshore wind farms. *J Atmos Ocean Technol*. 2010;27(8):1302-1317. doi:10.1175/2010JTECHA1398.1
3. Stevens RJAM, Meneveau C. Flow structure and turbulence in wind farms. *Ann Rev Fluid Mech*. 2017;49(1):311-339. doi:10.1146/annurev-fluid-010816-060206
4. Khanna S, Brasseur JG. Three-dimensional buoyancy- and shear-induced local structure of the atmospheric boundary layer. *J Atmos Sci*. 1998;55(5):710-743. doi:10.1175/1520-0469(1998)055%3C0710:TDBASI%3E2.0.CO;2
5. Kosovi B, Curry JA. A large eddy simulation study of a quasi-steady, stably stratified atmospheric boundary layer. *J Atmos Sci*. 2000;57(8):1052-1068.
6. Mason PJ, Derbyshire SH. Large-eddy simulation of the stably-stratified atmospheric boundary layer. *Bound-Layer Meteorol*. 1990;53(1):117-162.
7. Basu S, Portgel F. Large-eddy simulation of stably stratified atmospheric boundary layer turbulence: a scale-dependent dynamic modeling approach. *J Atmos Sci*. 2006;63(8):2074-2091.
8. Lu H, Porté-Agel F. Large-eddy simulation of a very large wind farm in a stable atmospheric boundary layer. *Phys Fluids*. 2011;23(6):065101. doi:10.1063/1.3589857
9. Hansen KS, Barthelme RJ, Jensen LE, Sommer A. The impact of turbulence intensity and atmospheric stability on power deficits due to wind turbine wakes at Horns Rev wind farm. *Wind Energy*. 2012;15(1):183-196. doi:10.1002/we.512
10. Dörenkämper M, Witha B, Steinfeld G, Heinemann D, Kühn M. The impact of stable atmospheric boundary layers on wind-turbine wakes within offshore wind farms. *J Wind Eng Ind Aerodyn*. 2015;144:146-153.
11. Abkar M, Porté-Agel F. Influence of atmospheric stability on wind-turbine wakes: a large-eddy simulation study. *Phys Fluids*. 2015;27(3):035104.
12. Magnusson M, Smedman A-S. Influence of atmospheric stability on wind turbine wakes. *Wind Eng*. 1994;18(3):139-152.
13. Vermeer LJ, Sørensen JN, Crespo A. Wind turbine wake aerodynamics. *Progr Aerosp Sci*. 2003;39(6):467-510.
14. Havelock T. The stability of motion of rectilinear vortices in ring formation. *The London, Edinburgh, and Dublin Phil Mag J Sci*. 1931;11(70):617-633.
15. Widnall SE. The stability of a helical vortex filament. *J Fluid Mech*. 1972;54(4):641-663.
16. Gupta BP, Loewy RG. Theoretical analysis of the aerodynamic stability of multiple, interdigitated helical vortices. *AIAA J*. 1974;12(10):1381-1387. doi:10.2514/3.49493
17. Okulov VL. On the stability of multiple helical vortices. *J Fluid Mech*. 2004;521:319-342.
18. Okulov VL, Sørensen JN. Stability of helical tip vortices in a rotor far wake. *J Fluid Mech*. 2007;576:1-25.
19. Sørensen JN, Naumov IV, Okulov VL. Multiple helical modes of vortex breakdown. *J Fluid Mech*. 2011;683:430-441.
20. Sørensen JN, Shen WZ. Numerical modeling of wind turbine wakes. *J Fluids Eng*. 2002;124(2):393-399.
21. Ivanell S, Mikkelsen R, Sørensen JN, Henningson D. Stability analysis of the tip vortices of a wind turbine. *Wind Energy*. 2010;13(8):705-715.
22. Sarmast S, Dadfar R, Mikkelsen RF, Schlatter P, Ivanell S, Sørensen JN, Henningson DS. Mutual inductance instability of the tip vortices behind a wind turbine. *J Fluid Mech*. 2014;755:705-731.
23. Nemes A, Sherry M, Jacono DL, Blackburn HM, Sheridan J. Evolution and breakdown of helical vortex wakes behind a wind turbine. In: *Journal of physics: Conference series*, Vol. 555 IOP Publishing; 2014:012077.
24. Kleusberg E, Benard S, Henningson DS. Tip-vortex breakdown of wind turbines subject to shear. *Wind Energy*. 2019;22(12):1789-1799.
25. Lignarolo LEM, Ragni D, Scarano F, Ferreira CJS, Van Bussel GJW. Tip-vortex instability and turbulent mixing in wind-turbine wakes. *J Fluid Mech*. 2015;781:467-493.
26. De Cillis G, Cherubini S, Semeraro O, Leonardi S, De Palma P. Pod-based analysis of a wind turbine wake under the influence of tower and nacelle. *Wind Energy*. 2021;24(6):609-633.
27. Deskos G, Laizet S, Palacios R. Winc3d: a novel framework for turbulence-resolving simulations of wind farm wake interactions. *Wind Energy*. 2020;23(3):779-794.
28. Bartholomew P, Deskos G, Frantz RAS, Schuch FN, Lamballais E, Laizet S. Xcompact3d: an open-source framework for solving turbulence problems on a Cartesian mesh. *SoftwareX*. 2020;12:100550.
29. Dairay T, Lamballais E, Laizet S, Vassilicos JC. Numerical dissipation vs. subgrid-scale modelling for large eddy simulation. *J Comput Phys*. 2017;337:252-274.

30. Deskos G, Laizet S, Piggott MD. Turbulence-resolving simulations of wind turbine wakes. *Renew Energy*. 2019;134:989-1002. doi:10.1016/j.renene.2018.11.084
31. Frantz RAS, Deskos G, Laizet S, Silvestrini JH. High-fidelity simulations of gravity currents using a high-order finite-difference spectral vanishing viscosity approach. *Comput Fluids*. 2021;221:104902.
32. Kravchenko AG, Moin P. On the effect of numerical errors in large eddy simulations of turbulent flows. *J Comput Phys*. 1997;131(2):310-322.
33. Lele SK. Compact finite difference schemes with spectral-like resolution. *J Comput Phys*. 1992;103(1):16-42.
34. Laizet S, Lamballais E. High-order compact schemes for incompressible flows: a simple and efficient method with quasi-spectral accuracy. *J Comput Phys*. 2009;228(16):5989-6015.
35. Laizet S, Li N. Incompact3d: a powerful tool to tackle turbulence problems with up to $O(10^5)$ computational cores. *Int J Numer Methods Fluids*. 2011;67:1735-1757.
36. Krogstad Per-AAge, Eriksen PE. Blind test calculations of the performance and wake development for a model wind turbine. *Renew Energy*. 2013;50:325-333.
37. Shen WZ, Mikkelsen R, Sørensen JN, Bak C. Tip loss corrections for wind turbine computations. *Wind Energy*. 2005;8(4):457-475.
38. Ali N, Cortina G, Hamilton N, Calaf M, Cal RB. Turbulence characteristics of a thermally stratified wind turbine array boundary layer via proper orthogonal decomposition. *J Fluid Mech*. 2017;828:175.
39. Sirovich L. Turbulence and the dynamics of coherent structures, parts I–III. *Quart Appl Math*. 1987;45(3):561-590.
40. Cal RB, Lebrón J, Castillo L, Kang HS, Meneveau C. Experimental study of the horizontally averaged flow structure in a model wind-turbine array boundary layer. *J Renew Sustain Energy*. 2010;2(1):013106.
41. VerHulst C, Meneveau C. Large eddy simulation study of the kinetic energy entrainment by energetic turbulent flow structures in large wind farms. *Phys Fluids*. 2014;26(2):025113.
42. Santoni C, Carrasquillo K, Arenas-Navarro I, Leonardi S. Effect of tower and nacelle on the flow past a wind turbine. *Wind Energy*. 2017;20(12):1927-1939.
43. Williams O, Hohman T, Van Buren T, Bou-Zeid E, Smits AJ. The effect of stable thermal stratification on turbulent boundary layer statistics. *J Fluid Mech*. 2017;812:1039-1075.

How to cite this article: Hodgkin A, Laizet S, Deskos G. Numerical investigation of the influence of shear and thermal stratification on the wind turbine tip-vortex stability. *Wind Energy*. 2022;1-20. doi:10.1002/we.2728